RSC Advances

PAPER

View Article Online
View Journal | View Issue

Cite this: *RSC Adv.*, 2023, **13**, 14131

A novel CEST-contrast nanoagent for differentiating the malignant degree in breast cancer†

Bixue Chen, [a] Xianfu Meng,[bc] Wanlu Wu,[a] Yuwen Zhang,[d] Lin Ma,[a] Kaidong Chen[a] and Xiangming Fang*[a]

Received 14th February 2023
Accepted 3rd May 2023

DOI: 10.1039/d3ra01006f

rsc.li/rsc-advances

Different subtypes of breast cancer (BCC) have variable degrees of malignancy, which is closely related to their extracellular pH (pH_e). Therefore, it is increasingly significant to monitor the extracellular pH sensitively to further determine the malignancy of different subtypes of BCC. Here, a L-arginine and Eu^{3+} assembled nanoparticle Eu^{3+}@L-Arg was prepared to detect the pH_e of two breast cancer models (TUBO is non-invasive and 4T1 is malignant) using a clinical chemical exchange saturation shift imaging technique. The experiments *in vivo* showed that Eu^{3+}@L-Arg nanomaterials could respond sensitively to changes of pH_e. In 4T1 models, the CEST signal enhanced about 5.42 times after Eu^{3+}@L-Arg nanomaterials were used to detect the pH_e. In contrast, few enhancements of the CEST signal were seen in the TUBO models. This significant difference had led to new ideas for identifying subtypes of BCC with different degrees of malignancy.

1 Introduction

Breast cancer (BCC), the second leading cause of cancer death, is the most common malignancy in women.[1–3] BCC is a highly heterogeneous disease at the molecular level,[4] which is divided into many subtypes.[5–7] The degree of malignancy varies between subtypes, and invasiveness is an important indicator of malignancy.[8,9] Therefore, it is essential to predict the invasiveness to further monitor the malignancy sensitively.

The heterogeneity of the tumor microenvironment with poor vascular perfusion, local hypoxia, anaerobic respiratory glycolysis and increased carbon flux leads to extracellular acidification of solid tumors.[10] Notably, acidification of the tumor microenvironment can occur at an early stage of the tumor, the avascular stage of pre-metastatic carcinoma *in situ* (CIS), where the greater the acidity of the CIS, the more likely it is to develop into a local infiltrate.[11] With intraductal hyperplasia, IDH gene mutations, *etc.*, tumor cells become more distant from the basement membrane and underlying blood vessels, and the relatively acidic pH promotes cancer progression by inducing migration and invasion.[12] One of the major pH-sensitive systems in cells is the actin cytoskeleton. The assembly of higher structures such as globular (G-actin) to filamentous (F-actin) and the process of disassembly of filamentous structures play different roles in the process and behavior of cancer cell vesicle transport, contraction, migration, invasion and metastasis. pH_e leads to significant differences in actin filament assembly and structure.[13] In addition to the initial assembly of actin filaments, metastasis requires remodeling of cell-matrix adhesion, a process necessitated by the increase in pH_i and the decrease in pH.[14] The key protein in this process is the focal adhesion protein talin, which reduces binding to actin filaments at $pH_i > 7.2$, a property that accelerates migration and facilitates the epithelial–mesenchymal transition (ECT) process.[15] The invasiveness is closely related to extracellular pH (pH_e), the lower the pH of BCC, the more invasive it is.[16–18] Therefore, monitoring the pH of BCC using clinical imaging techniques to further indicate the malignancy of BCC degree, is of increasing significance.

Chemical exchange saturation transfer (CEST) imaging is an important clinical magnetic resonance imaging (MRI) technique.[19–21] It is based on the chemical exchange between water protons and labile protons of the target including hydroxy, amino and amide protons.[22,23] The detection signal of CEST can be amplified by 10^2–10^4 compared to the traditional magnetic resonance spectrum (MRS) imaging technique.[19,24] In fact, the CEST signals strongly depend on the pH_e *in vivo*.[25–27] Hence CEST can be used to detect the pH.[24,28] However, endogenous labile protons have a small shift from the water peak,[24,29–31] which may result in an invalidity, such as non-

[a]*Department of Radiology, The Affiliated Wuxi People's Hospital of Nanjing Medical University, Wuxi, China. E-mail: xiangming_fang@njmu.edu.cn*

[b]*Department of Medical Ultrasound, Shanghai Tenth People's Hospital, School of Medicine, Tongji University, Shanghai, China*

[c]*Department of Materials Science, State Key Laboratory of Molecular Engineering of Polymers, Fudan University, Shanghai, China*

[d]*Institute of Science and Technology for Brain-Inspired Intelligence, Fudan University, Shanghai, China*

† Electronic supplementary information (ESI) available. See DOI: https://doi.org/10.1039/d3ra01006f

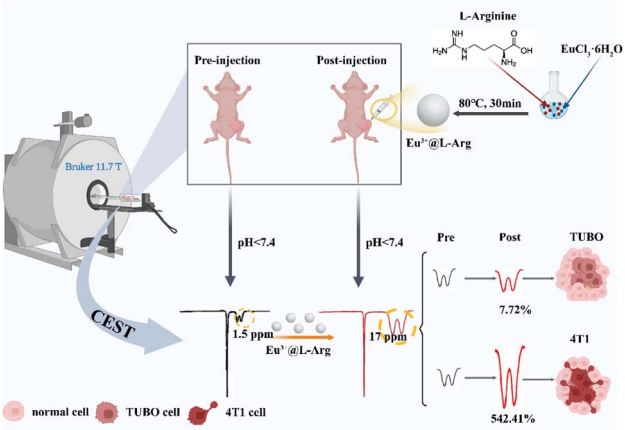

Scheme 1 Schematic diagram of pH detection CEST contrast agent for evaluating the malignancy of different subtypes of BCC, the area of the dashed line showing the CEST signal.

resonant direct saturation effects.[32] To solve this problem, paramagnetic CEST contrast agents were developed. However, small molecule contrast agents are readily metabolized,[29] which results in some signal variations during CEST scanning, causing significant interference in the accurate detection of pH_e. There is an urgent need to develop a new CEST contrast agent for the detection of pH_e accurately, allowing a real-time assessment of the malignancy of BCC.

Here, a paramagnetic nanoprobe was prepared to detect the pH_e of different types to further predict the malignancy of BCC. L-Arginine and Eu assembled nanoparticles, Eu^{3+}@L-Arg, were successfully prepared. Firstly, this probe could remain inside tumor for a long time, contributing to detecting the pH_e and avoiding the interference caused by metabolism. More importantly, the paramagnetic magnetic field of Eu^{3+} forms a strong electronic interaction with the amino hydrogen.[29,30,33,34] It induced the characteristic shift peak of arginine to low-field, which increased the chemical shift difference between amino and water molecules, further improving the CEST sensitivity (Scheme 1). Cells wound assays and the extracellular acidity ratio (ECAR) assays showed that 4T1 was more invasive and acid-producing than TUBO. *In vivo* and *in vitro* CEST experiments showed that the CEST signals increased with decreasing pH_e over time. No significant changes were seen in CEST for TUBO. In contrast, the CEST signals for 4T1 increased by 5.42 times, demonstrating a positive correlation between the degree of malignancy and the CEST signals. The use of CEST could help to identify the malignancy of different subtypes of BCC, bringing a great significance to the non-invasive clinical differentiation of tumor malignancy.

2 Experimental

2.1 Materials

Trihydroxy methane and europium chloride hexahydrate were both obtained from Aladdin (China). Sodium chloride was purchased from Sigma-Aldrich (US) and L-arginine was obtained from Adamas (Switzerland). Ethanol was obtained from generic reagents. All reagents were of analytical grade and could be used without further purification. MTT cell proliferation and cytotoxicity assay kit, Calcein/PI cell activity kit was obtained from Beyotime (China).

2.2 Instrumentation

Transmission electron microscopy (HTEM) and energy dispersive spectroscopy (EDS) images were obtained from a high contrast transmission electron microscope at 120.0 kV (Hitachi, Japan). Infrared spectra were determined with a Fourier transform infrared spectrometer (Thermo Fisher, US). X-ray diffractograms were obtained on a Rigaku D/MAX-2250V diffractometer. A thermogravimetric analyser (Mettler Toledo, Switzerland) was used for thermogravimetric analysis. Hydrodynamic radii and zeta potentials were collected by a Zetasizer Nano – ZS (Malvern Instruments, UK) enabling dynamic light scattering (DLS) analyser. Concentration of lanthanide metal ions were recorded using an Thermo Fisher iCAP 7400 (US) inductively coupled plasma spectrometer. T2 and CEST imaging was obtained using a Bruker 11.7 T magnetic resonance imaging instrument (US). Images were obtained using a Nikon Model Eclipse Ti2-E confocal microscope (Japan). MTT assays were performed with a Molecular Devices SpectraMax iD3 microplate instrument (US).

2.3 Synthesis of Eu^{3+}@L-Arg

Eu^{3+}@L-Arg nanoparticles were synthesized using a conventional hydrothermal method with some modifications. First, 1.8 mmol of L-arginine (L-Arg) and 2.0 mmol of europium chloride hexahydrate ($EuCl_3 \cdot 6H_2O$) were dissolved in 10 mL of a buffer with 50 mM tris(hydroxymethyl)aminomethane (Tris) and 100 mM sodium chloride (NaCl), followed by adding 0.084 mL HCl (0.1 mmol L^{-1}) to adjust the pH of the buffer to 7.4. The solution was then slowly stirred and heated to 80 °C, till to 30 min. The mixed solution was observed that the colour gradually changed from colourless to milky white. 10 mL of ethanol (C_2H_6O) was then added to break the emulsion, and Eu^{3+}@L-Arg nanoparticles were obtained after centrifugation. Finally, they were washed several times with deionized water and dispersed in 10 mL of deionized water.

2.4 Stability of Eu^{3+}@L-Arg

Eu^{3+}@L-Arg nanoparticles were dispersed in Hepes with different pH (5.6, 6.0, 6.4, 6.8, 7.2, 7.6) for 24 h. The hydrated particle size and zeta potential were measured and compared.

2.5 CEST imaging property of Eu^{3+}@L-Arg aqueous solution

500 μL Eu^{3+}@L-Arg aqueous solution of different concentrations were injected into the NMR tubes (Eu: 0, 8, 16, 31.25, 62.5, 125, 250, 500, 1000 μg mL^{-1}), and then the tubes were fixed in 1% agarose (37 °C, 50 mL). Eu^{3+}@L-Arg nanoparticles with different concentrations were imaged using CEST to validate the CEST imaging ability of Eu^{3+}@L-Arg nanoparticles, several buffers of 50 mM were prepared with Hepes and adjusted to pH = 5.6, 6.0, 6.4, 6.8, 7.2, 7.6 with NaOH (0.5 M). Eu^{3+}@L-Arg nanoparticles

were added into the above solutions with a resulting concentration of 62.5 μg mL^{-1} 500 μL aqueous solutions with different pH were removed, placed into NMR tubes and fixed in a centrifuge tube (50 mL), which filled with 1% agarose (37 °C) for T2 and CEST imaging.

T2 and CEST MRI were performed on a Bruker Biospin 11.7 T vertical bore scanner equipped with a 20 mm body transmit/receive coil. A modified T2 rapid acquisition with refocused echoes (RARE) sequence was used with magnetic field strength = 11.7 T, repetition time = 2500 ms, echo time = 26 ms, average = 2, slice thickness = 1 mm, layer spacing = 4 mm, field of view (FOV) = 100 × 100 mm. The total acquisition time was 2 min and 14 s. A modified CEST with ultra-short echo time (UTE) sequence was used with magnetic field strength = 11.7 T, repetition time = 50 ms, echo time = 0.4 ms, average = 4, slice thickness = 1.0 mm, layer spacing = 0.2 mm, FOV = 30 × 30 mm, matrix size = 100 × 100 mm, resolution = 0.25 × 0.25 mm, B_1 = 10 μT s^{-1}. The saturation offset frequencies were acquired from −30 to 30 ppm (with 2 ppm increments), with the water resonance frequency set at 0 ppm. The total acquisition time was 14 min and 58 s.

2.6 Cell culture

4T1 cells were purchased from Fu Heng Biotechnology Co., Ltd (China), and TUBO cells were purchased from Feng Hui Biological Co., Ltd (China). 4T1 cells were proliferated in culture medium of RPMI 1640 (Gibco), 5% fetal bovine serum (FBS, Gibco) and 1% penicillin/streptomycin (Gibco). TUBO cells were proliferated in culture medium of DMEM (Gibco), 5% FBS (Gibco) and 1% penicillin/streptomycin (Gibco). 4T1 and TUBO cells were incubated at 37 °C, 5% CO_2.

2.7 Cell migration assays

The wound healing of 4T1 cells and TUBO cells was evaluated by continuous observation of the scratches for 24 hours. The TUBO and 4T1 cells were seeded in 6-well plates. Cells were scratched with a 10 μL of needle to create wounds. Then the cells were washed with PBS to remove loose cellular debris. pH = 7.4 or 6.8 medium was added to the cells, then the cells were incubated at 37 °C and 5% CO_2 for 24 hours. As the cells migrated to fill the scratched area, images were captured with a confocal microscope and the distance between the edges was calculated using Image J software. The degree of wound closure was determined as:

$$\text{Wound closure (\%)} = 1 - (\text{wound width } t_x/\text{wound width } t_0) \times 100.$$

Wound width t_x means wound width at a given point in time (24 h in this text). Wound width t_0 means wound width at 0 times. All experiments were performed at least three times.

2.8 Extracellular acidity ratio (ECAR) measurement

TUBO and 4T1 cells were plated in a 4-well Seahorse XF24 cells culture microplate (3×10^4 cells per well), and incubated 24 h to allow adherence in a 5% CO_2 incubator. After 24 hours, pH measurements were performed with the Seahorse XF24 Extracellular Flux Analyzer (Seahorse, US). Basal values (glycolysis under normal conditions) were measured at 0–20 min, and the fluorescence intensity tested every 10 min on Seahorse (37 °C). 10 mM of glucose was added at 20 min for a total incubation of 5 min, and the fluorescence intensity were assayed each 10 min on Seahorse (37 °C). Oligomycin (1 μM, an inhibitor of oxidative phosphorylation) was added at 45 min for a total incubation of 10 min, and the fluorescence intensity tested every 10 min on Seahorse (37 °C). Finally, 2-DG (50 mM, glycolysis inhibitor) was added at 75 min, and the fluorescence intensity tested every 10 min on Seahorse (37 °C). The data were analysed with a Seahorse XF24 Wave software version Wave 2.2 (Agilent Technologies, US).

2.9 CEST MRI imaging capabilities *in vitro*

4T1 cells and TUBO cells were separated with 0.25% trypsin and washed three times with PBS. 4T1 and TUBO cells were suspended in culture fluid with pH = 7.4 at a concentration of 1×10^7 cells per mL for 24 h. Then 1 mL of the solutions were transferred into NMR tubes and fixed in 1% agarose. 500 μL Eu^{3+}@L-Arg nanoparticles (Eu: 62.5 μg mL^{-1}) was subsequently added. T2 and CEST scans were then performed with the same conditions as above.

2.10 CEST MRI imaging capabilities *in vivo*

All animal experiments had passed the animal ethical review (Fudan University 202203007S). Healthy nude mice (6 weeks, females) were randomly divided into two groups (9 per group) after one week of acclimatization. 1×10^6 4T1 cells and TUBO cells were detached and suspended in 100 μL of PBS, and injected into the skin of the right hind limb to form subcutaneous tumours, respectively. The whole procedure was operated under anaesthesia with 1.5% isoflurane. On day 5, 10 and 15 (n = 3) after inoculation of 4T1 and TUBO subcutaneous tumours, 50 μL of Eu^{3+}@L-Arg nanoparticles (Eu: 62.5 μg mL^{-1}) were injected into tumours by a 1 mL syringe. T2 and CEST MRI scans were performed before and after the injection.

T2 and CEST MRI were performed on a Bruker Biospin 11.7 T vertical bore scanner equipped with a 20 mm body transmit/receive coil. A T2 RARE sequence was used with magnetic field strength = 11.7 T, repetition time = 2500 ms, echo time = 30 ms, average = 2, slice thickness = 0.5 mm, layer spacing = 0.1 mm, FOV = 100 × 100 mm. The total acquisition time was 2 min and 49 s. A B_0 map was performed before the CEST imaging, which was done to make the magnetic field distribution more uniform and reduce artefacts (magnetic field strength = 11.7 T, repetition time = 20 ms, average = 2, slice thickness = 0.7 mm, layer spacing = 18.6 mm, FOV = 40 × 40 mm). A modified CEST sequence with ultra-short echo time (UTE) sequence was then used with magnetic field strength = 11.7 T, repetition time = 80 ms, echo time = 0.3 ms, average = 4, slice thickness = 3.0 mm, layer spacing = 5.5 mm, FOV = 40 × 40 mm, matrix size = 100 × 100 mm, resolution = 0.3 × 0.3 mm, B_1 = 10 μT s^{-1}. The saturation offset frequencies were acquired

from −30 to 30 ppm (with 2 ppm increments), with the water resonance frequency set at 0 ppm. The total acquisition time was 29 min and 12 s.

All CEST images were analysed using a self-made script in MATLAB (The MathWorks, Inc., Natick, MA, USA). For the *in vivo* images, the difference contrast map (ΔST%) was calculated on a per voxel basis by subtracting the ST contrast after and before nanomaterials injection. Three regions of interest (ROI) were taken in the area both before and after the nanomaterials were injected, and the values were averaged to reduce the errors caused by manual selection. The injected tissue area was normalized. The injected area was pseudo-colour stained, and the normal tissue signal was as 0.

2.11 MTT assay

Cytotoxicity was assayed by MTT. TUBO and 4T1 cells in logarithmic phase of growth were uniformly inoculated in 96-well cell culture plates (100 μL, 10 000 cells per well). After 24 hours of incubation, the culture solution was aspirated when the cells were at 60–70% density. Eu^{3+}@L-Arg solid were distributed in DMEM culture solution (Gibco) in order to prepare different concentrations of nanomaterial solutions (0, 3.125, 6.25, 12.5, 25, 50, 100, 200, 400, 800 μg mL^{-1}). Subsequently, different concentrations of Eu^{3+}@L-Arg solutions were added (100 μL) and co-incubated for 24 hours. The supernatant was aspirated and 100 μL of MTT (5 mg mL^{-1}) dilution was added to each well, and the cells were incubated for 4 h. Then 100 μL of formazan lysate was added into the wells, and the cells were incubated overnight at 37 °C in the incubator. Until the formazan was observed under an ordinary light microscope and found to be completely dissolved. The absorbance of each well was measured at 570 nm and the cell viability was obtained.

2.12 Calcein-AM/propidium iodide (PI) double stain

TUBO and 4T1 cells (20 000 cells) were inoculated on glass bottom cell culture dish ($\Phi = 15$ mm, NEST) and incubated for 24 h. 800 μg mL^{-1} of Eu^{3+}@L-Arg nanoparticles were added and the cell supernatant was discarded after co-culturing for 24 h. The cells were washed 3 times with PBS. Calcein AM/PI working solution was added and incubated for 30 min at 37 °C protected from light. Finally, the experimental results of the experimental and control groups were observed by laser confocal microscopy.

2.13 *In vivo* toxicity analysis

All animal experiments conformed to the guidelines of the Fudan University Animal Experimentation Ethics Committee (Fudan University 202203007S). Healthy mice (ICR, 20 g, 6 w, female) were divided into 3 groups (5 mice in each group). 20 μL of Eu^{3+}@L-Arg nanoparticles (Eu: 50 000 μg mL^{-1}) were injected intravenously into the mice in the experiment group. While the control group was injected with 20 μL of 0.9% NaCl accordingly. Mice in the experimental group were killed on day 3 and day 30 to study the short- and long-term toxicity. During this period, the body weight of the mice was also recorded. Isolated organs, including heart, liver, spleen, lungs and kidneys, were stained with haematoxylin and eosin (H&E) for histological analysis. In addition, blood analysis of the mice was also performed.

3 Results and discussion

3.1 Synthesis and characterization of Eu^{3+}@L-Arg

Eu^{3+}@L-Arg nanoparticles were synthesized by a facile hydrothermal method. A scheme of the synthesis of Eu^{3+}@L-Arg was shown in Fig. S1.† Eu^{3+}@L-Arg nanoparticles were successfully obtained by simply controlling the temperature and pH of the system. Transmission electron microscopy (TEM) measurements showed that the nanomaterials were monodispersed with a diameter of 120.5 nm (Fig. 1A), and high-resolution transmission electron microscopy (HRTEM) images showed distinct lattice fringe (Fig. 1B), which showed a great crystallinity. Energy dispersive spectroscopy (EDS) elemental analysis (Fig. S2†) and elements mapping (Fig. 1C) also confirmed that the nanoparticles were successfully acquired. Meanwhile, dynamic light scattering (DLS) showed that the nanomaterials had a hydrodynamic diameter of 176.9 nm (Fig. S3†) and the PDI was 0.095. In addition, X-ray photoelectron spectroscopy (XPS) (Fig. 1D and S4†) also demonstrated that Eu^{3+} was successfully coordinated to L-Arg. Fourier transform infrared (FTIR) spectra exhibited a red shift at 3000–3500 cm^{-1} after the co-ordination of Eu^{3+} with L-Arg (Fig. 1E), also indicating the successful preparation of Eu^{3+}@L-Arg. X-ray diffraction (XRD) showed a new peak (Fig. 1F) compared to L-Arg and Eu^{3+} mixed

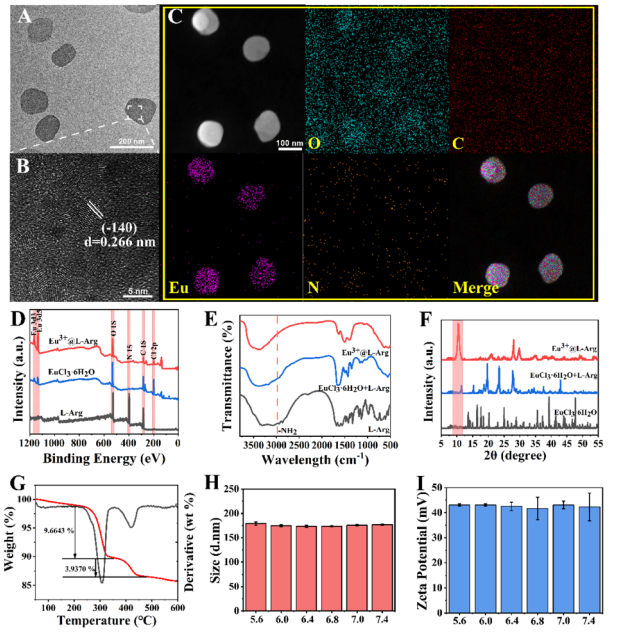

Fig. 1 Synthesis and characterization of Eu^{3+}@L-Arg. (A) TEM and (B) HRTEM images of Eu^{3+}@L-Arg. Scale bar: $A = 200$ nm, $B = 5$ nm; (C) elements mapping of Eu^{3+}@L-Arg (scans of related elements in yellow font: O, C, Eu, N). Scale bar = 100 nm; (D) XPS of L-Arg, $EuCl_3 \cdot 6H_2O$ and Eu^{3+}@L-Arg (O, C, Eu, N); (E) FTIR and (F) XRD spectra of L-Arg, L-Arg + $EuCl_3 \cdot 6H_2O$ and Eu^{3+}@L-Arg; (G) TGA of Eu^{3+}@L-Arg; (H) hydrodynamic diameter and (I) zeta potential of Eu^{3+}@L-Arg in aqueous solutions of different pH (5.6, 6.0, 6.4, 6.8, 7.0, 7.4) ($n = 3$, mean ± SD). All experiments were performed at least three times.

with L-Arg, which proved that the original crystal shape was changed by the collocation of Eu^{3+} with L-Arg. The results of thermogravimetric analysis (TGA) demonstrated a reduction in the mass of the nanomaterials (13.60% of total weight loss, Fig. 1G). All the experimental results suggested that the Eu^{3+}@L-Arg nanoparticles were synthesized. Considering the acidic microenvironment of BCC, it was essential to verify the stability of Eu^{3+}@L-Arg. In order to investigate the stability of Eu^{3+}@L-Arg nanoparticles in buffers of different pH, Eu^{3+}@L-Arg nanoparticles were dispersed in different pH buffers ranging from 5.6–7.4. The results showed that the hydrated particle size and zeta potential of Eu^{3+}@L-Arg nanoparticles did not change significantly in the buffers with different pH values after 24 h (Fig. 1H, I and S5†), which suggested the high stability of Eu^{3+}@L-Arg.

3.2 CEST ability of Eu^{3+}@L-Arg in aqueous solutions

Eu^{3+} belonged to the lanthanide metal ions and had a powerful paramagnetic effect.[31,35,36] This effect brought a favourable CEST imaging performance for Eu^{3+}@L-Arg nanoparticles. In order to explore the contrast property of paramagnetic nano-CEST contrast agents, T2 and CEST imaging were conducted firstly at different concentrations (0–1000 μg mL^{-1}) of Eu^{3+}@L-Arg nanomaterials. It was found that the T2 inversion time would be significantly shortened at high concentrations (62.5–1000 μg mL^{-1}), and the MRI could not pick up the CEST signal (Fig. S6†). Therefore, the optimal concentrations for imaging were explored (0–62.5 μg mL^{-1}, Fig. 2A). In the range of 0–62.5 μg mL^{-1}, the CEST signal of the Eu^{3+}@L-Arg nanomaterials became progressively stronger at 17.0 ppm (Fig. 2B). The magnetization transfer ratio asymmetry (MTR_{asym}) was obtained by asymmetric analysis[37,38] (Fig. 2C), the results showed that the signals were proportional to the concentrations of Eu^{3+}@L-Arg nanomaterials (Fig. 2D). By comparing the imaging ability of Eu^{3+}@L-Arg with L-Arg in aqueous solutions with different pH values (5.6–7.4), it was found that the chemical shift of L-Arg was closed to the water peak (Fig. S7†), which might bring some mistakes during detecting pH. In contrast, the chemical shift of Eu^{3+}@L-Arg was transferred to 17.0 ppm (Fig. 2B), and this attributed to the paramagnetic magnetic field of Eu^{3+} and the electron transfer of hydrogen ions.[34] This was a great help to improve the sensitivity of CEST imaging. Then, the capability of pH detection was further investigated (Fig. 2E). Based on the variations of the CEST Z-spectral in different pH aqueous solutions (Fig. 2F), MTR_{asym} peaks were calculated at 17.0 ppm (Fig. 2G). The relationship between the MTR_{asym} peaks measured at 17.0 ppm and the pH within the range of 5.6–7.4 was linear ($R^2 = 0.946$) (Fig. 2H), which demonstrated a great CEST imaging ability of Eu^{3+}@L-Arg nanomaterials to detect pH.

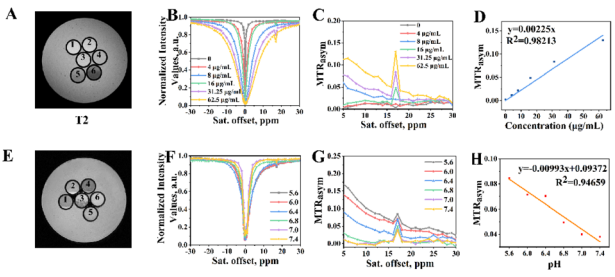

Fig. 2 (A) T2 images of different concentrations of Eu^{3+}@L-Arg nanomaterials (1–6: 0, 4, 8, 16, 31.25, 62.5 μg mL^{-1}); (B) Z spectrum and (C) MTR_{asym} images (17.0 ppm) of different concentrations (0, 4, 8, 16, 31.25, 62.5 μg mL^{-1}); (D) linear relationship chart between the concentration and the peak at 17.0 ppm of MTR_{asym}; (E) T2 images of Eu^{3+}@L-Arg (62.5 μg mL^{-1}) in different pH buffers (1–6: 5.6, 6.0, 6.4, 6.8, 7.0, 7.4); (F) the total Z-spectra and (G) MTR_{asym} profiles (17.0 ppm) of Eu^{3+}@L-Arg in different pH buffers; (H) linear relationship chart between MTR_{asym} peaks (17.0 ppm) and different pH values ($n = 3$, $B_0 = 11.7$ T, $B_1 = 10$ μT). All experiments were performed at least three times.

3.3 Investigation of invasiveness of the cells and CEST imaging ability of Eu^{3+}@L-Arg *in vitro*

The invasiveness was positively correlated with the malignancy of the tumour.[18] Thus, the relationship of TUBO and 4T1 cells between the invasiveness capacity and pH was measured. The results of invasiveness showed that TUBO and 4T1 cells cultured in normal medium (pH = 7.4) had a slower wound closure rate than those cultured in acidic culture solution (pH = 6.8) within 24 h (Fig. 3A). Fig. 3B demonstrated that a decreased pH_e resulted in increased cells invasiveness. At the same time, the above results showed that the invasiveness capability of 4T1 was much higher than TUBO, which indicated that 4T1 cells was more malignant than TUBO cells. To verify whether the pH_e could be used as a biological indicator of the invasiveness of

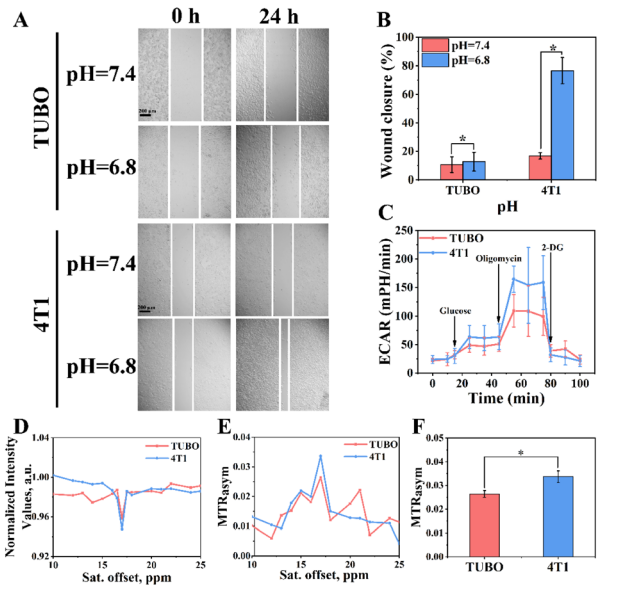

Fig. 3 (A) Images of TUBO and 4T1 cells invasiveness, cells were allowed to aggressive in normal and acidic medium for 24 hours after wounding (pH = 7.4 or 6.8). Scale bar = 200 μm; (B) histogram comparing (pH = 7.4 or 6.8, mean ± SD, $n = 3$, *$P < 0.05$); (C) the extracellular acidity ratio (ECAR) of TUBO and 4T1 cells in relation to time (0–100 min, mean ± SD, $n = 6$); (D) Z spectrum and (E) MTR_{asym} images of TUBO and 4T1 cells ($n = 3$, $B_0 = 11.7$ T, $B_1 = 10$ μT); (F) histogram of MTRasym at 17.0 ppm ($n = 3$, mean ± SD, $B_0 = 11.7$ T, $B_1 = 10$ μT). All experiments were performed at least three times.

BCC, the extracellular acidity ratio (ECAR) of TUBO and 4T1 cells during anaerobic respiration was measured. As shown in Fig. 3C, oligomycin (an inhibitor of the oxidative phosphorylation) was added at 45 min, and the aerobic respiration was inhibited in both of two cells. At this point, the ECAR was supplied by glycolysis totally. The results showed that the ECAR of 4T1 cells was 1.5 times higher than that in TUBO cells at 50–80 min, which was consistent with their invasiveness, demonstrating pH_e could be used to determine the invasiveness of BCC. Finally, Eu^{3+}@L-Arg nanomaterials were used to detect pH *in vitro*. 1×10^7 TUBO and 4T1 cells were suspended in culture fluid for 24 h, and then CEST imaging was performed after adding Eu^{3+}@L-Arg nanomaterials (Eu: 62.5 μg mL^{-1}). Z spectrum (Fig. 3D) and MTR_{asym} (Fig. 3E) images of 4T1 showed a stronger CEST signal at 17.0 ppm (2.64% of TUBO and 3.37% of 4T1, Fig. 3F). These results demonstrated that Eu^{3+}@L-Arg could respond sensitively to changes in pH *in vitro*.

3.4 CEST imaging ability of Eu^{3+}@L-Arg *in vivo*

Subsequently, the potential of Eu^{3+}@L-Arg nanoparticles for detecting the pH_e of BCC was assessed *in vivo*. CEST imaging was used to investigate the pH_e variation utilizing Eu^{3+}@L-Arg nanomaterials during the development (day 5, 10 and 15) of TUBO and 4T1 (Fig. S8†). Because only 1% of the intravenously injected nanomaterials could enter the tumour through the EPR (enhanced permeability and retention) effect,[39–41] we injected the nanomaterials directly into the tumour in order to achieve better imaging results.[42,43] Eu^{3+}@L-Arg nanomaterials (62.5 μg mL^{-1}, 50 μL) were injected into the tumours of TUBO and 4T1 at day 5, 10 and 15 after implantation of tumour cells. T2 and CEST scanning were undertook before and after the injection. For TUBO model at day 5, pseudoscalar maps (Fig. 4A), CEST Z-spectra signals (Fig. 4B) and MTR_{asym} (Fig. 4C) values at 17.0 ppm showed few changes, which indicated no significant change in pH_e of TUBO. As shown in Fig. 4D, the changes of CEST signal pre- and post-injection was 1.81% (SD = 0.19%). At the same time, with the size of TUBO increased, pseudoscalar maps (Fig. 4E and I), CEST Z-spectra signals (Fig. 4F and J) and MTR_{asym} values (Fig. 4G and K) of TUBO at day 10 and 15 still did not show noticeable signal changes after injection (Fig. 4H and L). The relative change ratio of CEST signal only increased by 7.72% (SD = 0.05%) and 4.49% (SD = 0.42%) at 17.0 ppm compared to the pre-injection, respectively (Fig. S9†). This might be attributed to the less malignancy and the slow growth of TUBO, which resulted in few changes of pH_e.

In contrast, pseudoscalar map (Fig. 5A) of day 5 of 4T1 models showed no significant signal change. But the pseudo-colour map signal of day 10 began to enhance after injection (Fig. 5E, yellow area). The CEST pseudo-colour map signal intensity further enhanced in post-injection region of day 15 (Fig. 5I, red area). The corresponding Z-spectrum signals (Fig. 5B, F and J) and MTR_{asym} values (Fig. 5C, G and K) were calculated according to the CEST pseudo-colour. The experimental data showed that the peak at 17.0 ppm increased with time, demonstrating that the pH_e decreased with 4T1 growing. The MTR_{asym} values at 17.0 ppm was plotted as a histogram

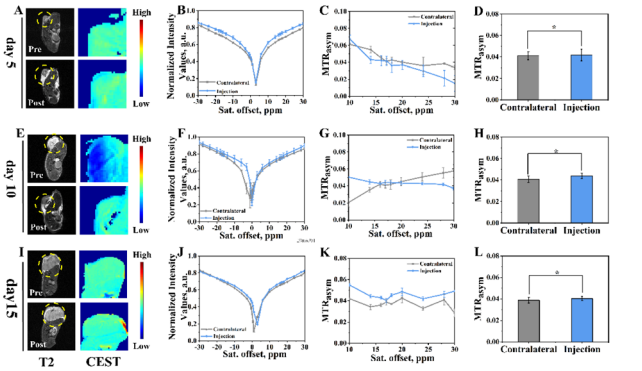

Fig. 4 Signal changes pre- and post-injection of Eu^{3+}@L-Arg in the TUBO model on day 5, day 10 and day 15, the dashed part was the corresponding tumour area for CEST pseudo-color processing; (A) T2 images and CEST MRI pseudo-colour maps pre- and post-injection of day 5; (B) pre- and post-injection CEST Z-spectra and (C) MTR_{asym} of day 5; (D) pre- and post-injection chemical shift histogram of day 5 (17.0 ppm, $n = 3$, $^*P > 0.05$, mean ± SD); (E) T2 images and CEST MRI pseudo-colour maps pre- and post-injection of day 10; (F) pre- and post-injection CEST Z-spectra and (G) MTR_{asym} of day 10; (H) pre- and post-injection chemical shift histogram of day 10 (17.0 ppm, $n = 3$, $^*P > 0.05$, mean ± SD); (I) T2 images and CEST MRI pseudo-colour maps pre- and post-injection of day 15; (J) pre- and post-injection CEST Z-spectra and (K) MTR_{asym} of day 15; (L) pre- and post-injection chemical shift histogram of day 15 (17.0 ppm, $n = 3$, $^*P > 0.05$, mean ± SD), ($B_0 = 11.7$ T, $B_1 = 10$ μT). All experiments were performed at least three times.

(Fig. 5D, H and L). As seen in Fig. 5D, the signal intensity of CEST increased by 0.70% of day 5 after injection (Fig. 5D) and by 2.86% of day 10 after injection (Fig. 5H), indicating that pH_e of

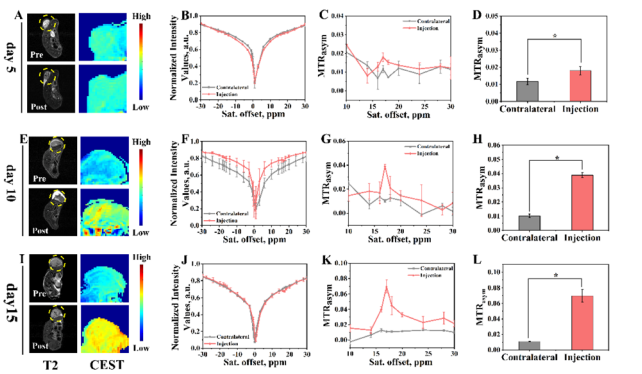

Fig. 5 Signal changes pre- and post-injection of Eu^{3+}@L-Arg in the 4T1 model on day 5, day 10 and day 15, the dashed part was the corresponding tumour area for CEST pseudo-color processing; (A) T2 images and CEST MRI pseudo-colour maps pre- and post-injection of day 5; (B) pre- and post-injection CEST Z-spectra and (C) MTR_{asym} of day 5; (D) pre- and post-injection chemical shift histogram of day 5 (17.0 ppm, $n = 3$, $^*P < 0.05$, mean ± SD); (E) T2 images and CEST MRI pseudo-colour maps pre- and post-injection of day 10; (F) pre- and post-injection CEST Z-spectra and (G) MTR_{asym} of day 10; (H) pre- and post-injection chemical shift histogram of day 10 (17.0 ppm, $n = 3$, $^*P < 0.05$, mean ± SD); (I) T2 images and CEST MRI pseudo-colour maps pre- and post-injection of day 15; (J) pre- and post-injection CEST Z-spectra and (K) MTR_{asym} of day 15; (L) pre- and post-injection chemical shift histogram of day 15 (17.0 ppm, $n = 3$, $^*P < 0.05$, mean ± SD), ($B_0 = 11.7$ T, $B_1 = 10$ μT). All experiments were performed at least three times.

day 10 was lower than day 5. The CEST signal intensity of day 15 increased by 5.89% (Fig. 5L). The relative change ratio of CEST signal increased by 58.55% (SD = 0.37%), 283.63% (SD = 0.19%) and 542.41% (SD = 0.87%) at 17.0 ppm compared to the pre-injection, respectively (Fig. S10†). This might be due to the fact that 4T1 grew more faster, which led to the insufficient oxygen supply and anaerobic glycolysis in tumour, further resulting in an acidic environment.[24,30,35] The post-injection CEST signal of day 5, day 10 and day 15 results demonstrated an efficient ability of Eu^{3+}@L-Arg nanoparticles to detect pH favourably *in vivo*.

3.5 Biosafety of Eu^{3+}@L-Arg

Firstly, the MTT assay was conducted to investigate the cytotoxicity on 4T1 and TUBO. As shown in Fig. S11A and B,† it was obviously observed that the survival rate was still more than 75% even in a high concentration (Eu: 800 μg mL^{-1}). Furthermore, calcein-AM (Calcein-AM) and propidium iodide (PI) assay was implemented to explore the survival. After co-culture of two cells with Eu^{3+}@L-Arg nanoparticles (Eu: 800 μg mL^{-1}) for 24 h, the number of dead cells in control and experimental groups was not considerably (Fig. S12†), demonstrating a great cell safety potential.[44–46]

Subsequently, their toxicity *in vivo* was further investigated. Eu^{3+}@L-Arg aqueous solution (Eu: 3000 μg mL^{-1}, 1 mL) (experimental group) or 0.9% physiological saline (control group) was intravenously injected into three groups of healthy ICR mice for short-term (day 3) and long-term (day 30) potential toxicity studies. The changes in body weight and physiological activity were observed in the control and day 30 groups, respectively. Apparently, there was no obvious difference in the trend of body weight changes between two groups (Fig. S13†). Furthermore, the serum biochemical parameters and blood biochemical parameters of the three groups (control, day 3, day 30) also showed the biosafety and low toxicological property of Eu^{3+}@L-Arg (Fig. S14†). The results of haematoxylin–eosin (H&E) staining also demonstrated few physiological changes in the heart, liver, spleen, lungs and kidneys (Fig. S15†). All of the above results demonstrated the positive biosafety of Eu^{3+}@L-Arg *in vivo*.

4 Conclusions

In summary, Eu^{3+}@L-Arg nanoparticles were synthesized to detect pH_e of different types of BCC to further predict the malignancy of BCC. Eu^{3+}@L-Arg nanoprobes had good biocompatibility and low toxicity. Cellular wound experiments showed that 4T1 was more invasive than TUBO, demonstrating that 4T1 was more malignant. ECAR experiments shown that 4T1 had a higher acid production rate. CEST experiments *in vitro* showed that the CEST signals were stronger in 4T1 than TUBO after culturing 24 h, indicating that the pH_e of 4T1 was lower than TUBO at this time. This demonstrated that the signal intensity of CEST was positively correlated with its invasive ability, thus enabling the determination of the malignancy of BCC. In the early stages of tumour development, the pH of the tumour microenvironment was changed.[11] As the tumour progresses, the solid tumour had an insufficient supply of oxygen and blood flow, and the acidic substances accumulated inside the tumour gradually increase. This caused the pH inside the tumour to decrease continuously.[10,47] The results of CEST experiments *in vivo* showed that the CEST signals of both 4T1 and TUBO increased to different degrees with the accumulation of acid in the BCC microenvironment (day 5, day 10 and day 15). But the CEST signals of 4T1 were stronger than TUBO (542.41% of 4T1 and 7.72% of TUBO), due to the greater malignancy of 4T1, and its higher acid production capacity (150 mpH per min of 4T1 and 100 mpH per min of TUBO). Thus, as the time of tumours grew longer, and the tumours were more acidic inside, 4T1 produced a stronger CEST signal after nanomaterial injection. In conclusion, the Eu^{3+}@L-Arg nanoprobe was sensitive in response to pH_e, which was positively correlated with the invasiveness of the BCC, which in turn was an important marker of malignancy. The use of the Eu^{3+}@L-Arg nanoprobe therefore helped CEST imaging to discriminate between subtypes with different degrees of malignancy. However, the mechanism by which the nanomaterials respond to pH_e *in vivo* is not yet known to us. Also, only the breast cancer models were used in this paper for validation, and was not extended to other cancer models for exploration. If validated in other cancer models, it will provide new ideas for non-invasive identification of tumour subtypes, and provide a more early and favourable diagnostic approach for personalized clinical treatment.

Author contributions

Bixue Chen: conceptualisation, data curation, investigation, methodology writing-original draft. Xianfu Meng: conceptualisation, investigation, methodology writing-original draft. Wanlu Wu: supervision, data curation. Yuwen Zhang: data curation, formal analysis, investigation, methodology. Lin Ma: project administration, supervision. Kaidong Chen: investigation, methodology. Xiangming Fang: conceptualization, funding acquisition, project administration, writing – original draft. All authors contributed to the article and approved the submitted version.

Conflicts of interest

There are no conflicts to declare.

Acknowledgements

The authors would greatly acknowledge Wuxi Medical Innovation Team Program (CXTD002), Natural Science Foundation of Jiangsu Province (BK20191143), National Natural Science Foundation of China (81271629), and the Medical Expert Team Program of Wuxi Taihu Talent Plan 2021 and ZJLab.

References

1 C. DeSantis, R. Siegel, P. Bandi and A. Jemal, *Ca-Cancer J. Clin.*, 2011, **61**, 409–418.

2 U. Veronesi, P. Boyle, A. Goldhirsch, R. Orecchia and G. Viale, *Lancet*, 2005, **365**, 1727–1741.
3 J. Ferlay, M. Colombet, I. Soerjomataram, D. M. Parkin, M. Piñeros, A. Znaor and F. Bray, *Int. J. Cancer*, 2021, **149**, 778–789.
4 Y. Gong, P. Ji, Y. S. Yang, S. Xie, T. J. Yu, Y. Xiao, M. L. Jin, D. Ma, L. W. Guo, Y. C. Pei, W. J. Chai, D. Q. Li, F. Bai, F. Bertucci, X. Hu, Y. Z. Jiang and Z. M. Shao, *Cell Metab.*, 2021, **33**, 51–64.
5 A. Goldhirsch, W. C. Wood, A. S. Coates, R. D. Gelber, B. Thürlimann and H. J. Senn, *Ann. Oncol.*, 2011, **22**, 1736–1747.
6 T. Sørlie, C. M. Perou, R. Tibshirani, T. Aas, S. Geisler, H. Johnsen, T. Hastie, M. B. Eisen, M. van de Rijn, S. S. Jeffrey, T. Thorsen, H. Quist, J. C. Matese, P. O. Brown, D. Botstein, P. E. Lønning and A.-L. Børresen-Dale, *Proc. Natl. Acad. Sci. U. S. A.*, 2001, **98**, 10869–10874.
7 K. M. Turner, S. K. Yeo, T. M. Holm, E. Shaughnessy and J. L. Guan, *Am. J. Physiol.: Cell Physiol.*, 2021, **321**, C343–c354.
8 D. L. Page, *The American Journal of Surgical Pathology*, 1991, **15**, 334–349.
9 H. J. Burstein, G. Curigliano, B. Thürlimann, W. P. Weber, P. Poortmans, M. M. Regan, H. J. Senn, E. P. Winer and M. Gnant, *Ann. Oncol.*, 2021, **32**, 1216–1235.
10 D. Hanahan and R. A. Weinberg, *Cell*, 2011, **144**, 646–674.
11 M. Barathova, M. Takacova, T. Holotnakova, A. Gibadulinova, A. Ohradanova, M. Zatovicova, A. Hulikova, J. Kopacek, S. Parkkila, C. T. Supuran, S. Pastorekova and J. Pastorek, *Br. J. Cancer*, 2008, **98**, 129–136.
12 A. J. Bradley, Y. Y. Lim and F. M. Singh, *Clin. Radiol.*, 2011, **66**, 1129–1139.
13 N. Ishiyama, R. Sarpal, M. N. Wood, S. K. Barrick, T. Nishikawa, H. Hayashi, A. B. Kobb, A. S. Flozak, A. Yemelyanov, R. Fernandez-Gonzalez, S. Yonemura, D. E. Leckband, C. J. Gottardi, U. Tepass and M. Ikura, *Nat. Commun.*, 2018, **9**, 5121.
14 S. P. Denker and D. L. Barber, *J. Cell Biol.*, 2002, **159**, 1087–1096.
15 J. Srivastava, G. Barreiro, S. Groscurth, A. R. Gingras, B. T. Goult, D. R. Critchley, M. J. Kelly, M. P. Jacobson and D. L. Barber, *Proc. Natl. Acad. Sci. U. S. A.*, 2008, **105**, 14436–14441.
16 D. E. Korenchan and R. R. Flavell, *Cancers*, 2019, **11**, 1026.
17 M. Damaghi, J. W. Wojtkowiak and R. J. Gillies, *Front. Physiol.*, 2013, **4**, 370.
18 A. Anemone, L. Consolino, L. Conti, P. Irrera, M. Y. Hsu, D. Villano, W. Dastru, P. E. Porporato, F. Cavallo and D. L. Longo, *Br. J. Cancer*, 2021, **124**, 207–216.
19 P. C. M. van Zijl, W. W. Lam, J. Xu, L. Knutsson and G. J. Stanisz, *NeuroImage*, 2018, **168**, 222–241.
20 K. M. Jones, A. C. Pollard and M. D. Pagel, *J. Magn. Reson. Imaging*, 2018, **47**, 11–27.
21 S. D. Wolff and R. S. Balaban, *Magn. Reson. Med.*, 1989, **10**, 135–144.
22 R. G. Bryant, *Annu. Rev. Biophys. Biomol. Struct.*, 1996, **25**, 29–53.
23 P. C. van Zijl, J. Zhou, N. Mori, J. F. Payen, D. Wilson and S. Mori, *Magn. Reson. Med.*, 2003, **49**, 440–449.
24 J. Zhou, J. F. Payen, D. A. Wilson, R. J. Traystman and P. C. van Zijl, *Nat. Med.*, 2003, **9**, 1085–1090.
25 E. Liepinsh and G. Otting, *Magn. Reson. Med.*, 1996, **35**, 30–42.
26 K. M. Ward and R. S. Balaban, *Magn. Reson. Med.*, 2000, **44**, 799–802.
27 L. Consolino, A. Anemone, M. Capozza, A. Carella, P. Irrera, A. Corrado, C. Dhakan, M. Bracesco and D. L. Longo, *Front. Oncol.*, 2020, **10**, 161.
28 A. Anemone, L. Consolino, F. Arena, M. Capozza and D. L. Longo, *Cancer Metastasis Rev.*, 2019, **38**, 25–49.
29 I. Hancu, W. T. Dixon, M. Woods, E. Vinogradov, A. D. Sherry and R. E. Lenkinski, *Acta Radiol.*, 2010, **51**, 910–923.
30 S. Zhang, M. Merritt, D. E. Woessner, R. E. Lenkinski and A. D. Sherry, *Acc. Chem. Res.*, 2003, **36**, 783–790.
31 M. Woods, D. E. Woessner, P. Zhao, A. Pasha, M. Y. Yang, C. H. Huang, O. Vasalitiy, J. R. Morrow and A. D. Sherry, *J. Am. Chem. Soc.*, 2006, **128**, 10155–10162.
32 S. J. Ratnakar, M. Woods, A. J. Lubag, Z. Kovacs and A. D. Sherry, *J. Am. Chem. Soc.*, 2008, **130**, 6–7.
33 S. J. Ratnakar, S. Viswanathan, Z. Kovacs, A. K. Jindal, K. N. Green and A. D. Sherry, *J. Am. Chem. Soc.*, 2012, **134**, 5798–5800.
34 S. Karan, M. Y. Cho, H. Lee, H. S. Park, E. H. Han, Y. Song, Y. Lee, M. Kim, J. H. Cho, J. L. Sessler and K. S. Hong, *J. Med. Chem.*, 2022, **65**, 7106–7117.
35 L. Zhang, A. F. Martins, P. Zhao, Y. Wu, G. Tircsó and A. D. Sherry, *Angew. Chem., Int. Ed. Engl.*, 2017, **56**, 16626–16630.
36 S. Lacerda and É. Tóth, *ChemMedChem*, 2017, **12**, 883–894.
37 P. C. van Zijl and N. N. Yadav, *Magn. Reson. Med.*, 2011, **65**, 927–948.
38 T. Gao, C. Zou, Y. Li, Z. Jiang, X. Tang and X. Song, *Int. J. Mol. Sci.*, 2021, **22**, 11559.
39 J. Fang, W. Islam and H. Maeda, *Adv. Drug Delivery Rev.*, 2020, **157**, 142–160.
40 H. Maeda, H. Nakamura and J. Fang, *Adv. Drug Delivery Rev.*, 2013, **65**, 71–79.
41 Y. Matsumura and H. Maeda, *Cancer Res.*, 1986, **46**, 6387–6392.
42 C. Zhu, Q. Ma, L. Gong, S. Di, J. Gong, Y. Wang, S. Xiao, L. Zhang, Q. Zhang, J. J. Fu, D. Lu and Z. Lin, *Acta Biomater.*, 2022, **141**, 429–439.
43 J. Chen, M. Lv, X. Su, S. Wang, Y. Wang, Z. Fan, L. Zhang and G. Tang, *Int. J. Nanomed.*, 2022, **17**, 5605–5619.
44 H. Li, H. Zhang, X. He, P. Zhao, T. Wu, J. Xiahou, Y. Wu, Y. Liu, Y. Chen, X. Jiang, G. Lv, Z. Yao, J. Wu and W. Bu, *Adv. Mater.*, 2023, e2211597, DOI: **10.1002/adma.202211597**.
45 X. Meng, H. Zhang, M. Zhang, B. Wang, Y. Liu, Y. Wang, X. Fang, J. Zhang, Z. Yao and W. Bu, *Adv. Sci.*, 2019, **6**, 1901214.
46 Y. Liu, S. Zhai, X. Jiang, Y. Liu, K. Wang, C. Wang, M. Zhang, X. Liu and W. Bu, *Adv. Funct. Mater.*, 2021, **31**, 2010390.
47 L. Barthel, M. Hadamitzky, P. Dammann, M. Schedlowski, U. Sure, B. K. Thakur and S. Hetze, *Cancer Metastasis Rev.*, 2022, **41**, 53–75.